Journal of Archaeological Science 36 (2009) 1857–1868

Contents lists available at ScienceDirect

Journal of Archaeological Science

journal homepage: http://www.elsevier.com/locate/jas

An X-ray Diffraction (XRD) and X-ray Fluorescence (XRF) investigation in human and animal fossil bones from Holocene to Middle Triassic

Giampaolo Piga [a,*], Andrés Santos-Cubedo [b], Salvador Moya Solà [b], Antonio Brunetti [c], Assumpciò Malgosa [a], Stefano Enzo [d]

[a] Unitat d'Antropologia, Department de Biologia Animal, Biologia Vegetal i Ecologia, Universitat Autònoma de Barcelona, Edifici C, 08193 Bellaterra, Barcelona, Spain
[b] Institut Català de Paleontologia C/Escola Industrial, 23, E-08201 Sabadell, Barcelona, Spain
[c] Struttura Dipartimentale di Matematica e Fisica, Università di Sassari, via Vienna n. 2, I-07100 Sassari, Italy
[d] Dipartimento di Chimica, Università di Sassari, via Vienna n. 2, I-07100 Sassari, Italy

ARTICLE INFO

Article history:
Received 28 November 2008
Received in revised form
15 March 2009
Accepted 10 April 2009

Keywords:
X-ray Diffraction
Rietveld method
X-ray Fluorescence
Human and animal fossil bones
Bone diagenesis

ABSTRACT

We examined by Rietveld refinement of X-ray Diffraction patterns a series of 61 human and animal fossil bones in an age range from present time to Middle Triassic (around 245 Ma). This approach, supplemented by elemental analysis according to X-ray Fluorescence, has permitted to obtain a quantitative evaluation of the mineralogical phases in the specimens, thus allowing to reconstruct the mineralization process involved. Concerning the apatite phase, after adopting a monoclinic geometry for the unit cell, the method permits to determine with fair degree of precision the unit cell volume, which is found to decrease in relatively short geological times as a function of the fluorine substitution process for the hydroxyl group –OH. After excluding the role of a high-temperature fire treatment to the bones, it is found that a certain linear correlation may exist over the geological time scale involved between the age of the specimen and the average crystallite size. This observation permits to use the XRD pattern as an evaluation of the age of the fossil, although the stratigraphic observations, where available, remain as the main reliable source for dating such biomaterials. The uncertainty related to this age estimation may be hardly better than 15–20% in absolute, because of various assumptions involved in the XRD methodology used and in the variability of the burial environment that may be subjected to discontinuous changes over the very long time of deposition.

1. Introduction

Animal and human bones which are brought to light after a wide time scale range constitute important witnesses to trace the diagenetic changes. Depending on the burial environment the bones are subjected to several changes. First, the organic matter separates from the inorganic biomineral of bones known as apatite, subsequently mineralization can occur, possibly accompanied by dissolution according to heterogeneous acid–base chemical reactions.

In fact, it is also recognized that an alkaline environment may help the preservation of bones.

In the hypothesis that the post-mortem and burial changes (diagenesis) are associated to crystallinity of apatite from XRD, it was suggested to relate this index to the age. This correlation was found by Bartsiokas and Middleton (1992) after examining 15 bony specimens, two of which were rejected from the analysis because of their "state of histological conservation". In the hypothesis of a first-order kinetics process, the relationship was expressed by a linear regression between the crystallinity index (CI) and logarithm of age.

Note that the term crystallinity is instinctively intended as degree of organization of the hydroxylapatite phase (HA) on an atomic scale (Handschin and Stern, 1992).

Soon after, Person et al. (1995, 1996) defined a slightly different CI after considering a larger number of specimens of various provenance and age. They did not observe any significant correlation between the increase in the CI and the age of the sample, even in bones from the same locality. More recently (Farlow and Argast, 2006) it was reported further data consistent with the results of Person et al. (1995, 1996) in showing no relationship between bone crystallinity and age. However, for late Pleistocene and younger specimens, their data were consistent with the observations of Bartsiokas and Middleton (1992) and Sillen and Parkington (1996) for mammalian bone.

* Corresponding author.
E-mail address: kemiomara@yahoo.it (G. Piga).

0305-4403/$ – see front matter © 2009 Elsevier Ltd. All rights reserved.
doi:10.1016/j.jas.2009.04.013

As with the mammalian bone studied by those workers, the turtle shell material of Farlow and Argast showed a clear increase in bone crystallinity with age.

Actually, both crystallization indexes used by Bartsiokas and Middleton (1992) and by Person et al. (1995, 1996) are a measure of the relative intensities of some peak profiles and the valleys between them, analogously to the splitting factor similarly used in Infrared Spectroscopy of bones (Weiner and Bar-Yosef, 1990).

Rather than referring to the crystallinity of HA, we estimate a valid and more rigorous approach to evaluate the X-ray peak sharpening of HA bones in terms of the average size of coherently diffracting domains (otherwise referred to as crystallites) and/or average imperfection density, also called lattice disorder or microstrain (Chipera and Bish, 1991). These parameters supply a means to define numerically the organization of bones in an atomic scale. The type of lattice disorder is in turn quite complex. First of all the natural apatites, are usually regarded as crystal of hexagonal geometry where calcium cations of pure hydroxylapatite $Ca_5(PO_4)_3OH$ may be replaced by other alkaline and transitional cations.

Second, the phosphate groups may be replaced by carbonatic CO_3^{2-} groups. Third, replacement of hydroxyl groups with fluorine (fluoritization) is also known to occur. Note that carbonate fluorapatite [$Ca_5(PO_4,CO_3)_3(F)$] having more than 1 wt% of fluorine and carbon dioxide is regarded as francolite, while the carbonate hydroxyapatite with a fluorine content which does not exceed 1 wt% is called dahllite (Hubert et al., 1996).

Certainly, mechanism of cation exchange occurring both *ante-* and *post-mortem* may affect the degree of lattice disorder. A possible consequence of this is that the hexagonal lattice is deformed to a certain extent. Following Elliott et al. (1973) a monoclinic description of the unit cell of apatite (Space Group $P2_1/c$, 4 molecular units) was suggested rather than the hexagonal cell of S. G. $P6_{3/m}$ with two molecules of HA. In fact, the lattice parameter of the monoclinic phase a_M coincides with that of the hexagonal phase a_H, but b_M is ca $2 \times a_H$, while $c_M = c_H$ and $\beta_M \approx 120^\circ$.

Thus, the monoclinic unit cell volume of monoclinic structure V_M is about twice that of the hexagonal structure V_H. As a further consequence, in real bone samples, the X-ray peak positions may change slightly depending from the degree of foreign atomic substitution in the lattice which affects the lattice parameters. At parity of domain size extension, the measure of the crystallinity index CI is then expected to change. In any case, the quantitative evaluation of phases, their lattice parameters and their average coherent diffraction domain size may be obtained by applying the Rietveld method (Rietveld, 1967), as it was suggested by Michel et al. (1996). This is an efficient approach that evaluates quantitatively the amount, structure and microstructure parameters of mineralogical phases keeping also into account the instrumental parameters. While the average crystallite size parameter (also referred to as domain size) does not depend from the order of reflections, the lattice strain does. This measure should be considered more reliable because it uses the full XRD pattern and not a restricted angular range in correspondence of the most intense overlapped peaks. We have recently applied the Rietveld refinement method to follow the crystallization phenomena induced by heat treatment in human bones to verify whether the bodies were subjected to burning (Piga et al., 2008a,b). In a similar way we are applying here the Rietveld refinement method in a collection of 61 specimens of various fossils attributed from Holocene up to Middle Triassic (around 245 Ma). To better validate/reject a correlation between the average crystallite size and/or unit cell volume as a function of age in this study we are paying attention to the mineralogical phase constitution of bone specimens and to the structural and microstructural properties of the common apatite phase as inspected by powder XRD. Several specimens were also supplemented with the elemental composition by X-ray Fluorescence analysis (XRF).

2. Materials and methods

Table 1 is a list of the 61 specimens here studied which are coming from Spain, Italy, U.K. and Portugal. In the collection of these specimens an effort was made to reach a distribution as homogeneously as possible in the age range from present times back to Middle Triassic. All received fossils were looking like stones of irregular shape with volume 3–4 cm^3. The fossils were powdered to prepare specimens for X-ray Diffraction (XRD) and X-ray Fluorescence (XRF) investigations.

The XRD patterns were recorded overnight using Bruker D8, Philips PW-1050 and Siemens D-500 diffractometers in the Bragg–Brentano geometry with CuKα radiation ($\lambda = 1.54178$ Å).

The goniometers were equipped with graphite monochromators in the diffracted beam. The X-ray generator worked at a power of 40 kV and 30 mA and the resolution of the instruments (divergent and antiscatter slits of 0.5°) was determined using α-SiO_2 and α-Al_2O_3 standards free from the effect of reduced crystallite size and lattice defects. The powder patterns were collected in the angular range 10°–140° in 2θ, with counting time of 40 s per point and were analysed according to the Rietveld method (Rietveld, 1967). This approach consists in a structure refinement method, that is, the raw intensity data of an XRD pattern are compared with the diffraction results from numerical computation of each mineralogical phase which is supposed to be present in the specimen (model). The agreement between experiment and computation depends on one hand from the quality of intensity data and on the other hand from the pertinent model of hypothesized phase structure and constitution. The phase constitution is validated with high reliability by assessing typical sequence of line profiles and relative intensities which are taken as fingerprint of the substance.

The "best" final solution to this problem is automatically optimized on the basis of indicator and agreement factors consisting in the minimization of the sum of squared difference between calculated and experimental data points. Because the numbers for agreement factors are blind to a certain extent, it is customary to report at the end of the refinement (fit) the residual function i.e., deviations of model from experiment across the whole range of the pattern.

Because the intensities of the model are determined using the crystallographic rules, in turn based on geometry properties and electronic (and/or atomic) densities, the Rietveld method does not necessarily require any internal calibration standard for determining the amount of each phase, thus minimizing the work on sample preparation.

Among the programs available in the literature for this type of analysis we have used the programme MAUD (Lutterotti et al., 1998) which was preferred because it takes into account the instrument broadening (determined separately using a standard) directly in the proposed numerical solution. This permits to verify the validity of the final overall model in the domain of experimental data, without the need of any further off-program analysis of refined data that may imply new or different assumptions deviating from the experiment.

XRF-measurements have been carried out by using a portable equipment composed of an X-ray tube (molybdenum anode, Oxford Instruments) working at 25 kV and 0.1 mA.

An aluminium collimator 1 cm long and with an internal hole 1 mm in diameter permits to irradiate an area of about 0.2 cm^2 of the object to be analysed, at a distance tube window-sample of

Table 1
List of the bone specimens with geological period, classification and provenance location.

Sample	System period [series epoch/stage age/age (Ma)]	Classification	Provenance
Menorca IPS35594	Middle Triassic (Anisian) (245 Ma)	Seymouriamorpha	Menorca – Spain
La Mora	Middle Triassic (Anisian) (245–241 Ma)	*Eryosuchus* sp.	Menorca – Spain
Menorca IPS37436	Middle Triassic (Anisian/Ladinian) (ca 240 Ma)	Amphibian	Menorca – Spain
Losilla	Upper Jurassic–Lower Cretaceous (150–145 Ma)	Dinosaur (Eusauropoda)	Alpuente (Valencia) – Spain
Aras De Alpuente	Upper Jurassic–Lower Cretaceous (150–145 Ma)	Dinosaur (Eusauropoda)	Alpuente (Valencia) – Spain
La Ventura	Upper Jurassic–Lower Cretaceous (150–145 Ma)	Dinosaur (Eusauropoda)	Alpuente (Valencia) – Spain
El Collado	Upper Jurassic–Lower Cretaceous (150–145 Ma)	Dinosaur	Alpuente (Valencia) – Spain
Patiras	Lower Cretaceous (Barremian)	Dinosaur	Todolella (Castellón) – Spain
CL42	Lower Cretaceous (Barremian)	Dinosaur (Euornithopoda)	Portell (Castellón) – Spain
La Fita	Lower Cretaceous (Barremian)	Dinosaur (Euornithopoda)	Cinctorres (Castellón) – Spain
La Cuba	Lower Cretaceous (Barremian)	Dinosaur	Portell (Castellón) – Spain
SAV67	Lower Cretaceous (Aptian)	Dinosaur (Eusauropoda)	Morella (Castellón) – Spain
Povet	Lower Cretaceous (Aptian)	Dinosaur (Euornitopodo)Ornithopoda	Morella (Castellón) – Spain
Comptadors_A1	Lower Cretaceous (Aptian)	Dinosaur	Cinctorres (Castellón) – Spain
Todolella_1	Lower Cretaceous (Aptian)	Dinosaur	Todolella (Castellón) – Spain
Camino	Lower Cretaceous (Aptian)	Dinosaur	Morella (Castellón) – Spain
EAP 40-39	Lower Cretaceous (Aptian)	Dinosaur	Morella (Castellón) – Spain
Qurolles-M	Lower Cretaceous (Aptian)	Dinosaur (Euornithopoda)	Portell (Castellón) – Spain
MC1–5	Lower Cretaceous (Aptian)	Dinosaur (Euornithopoda)	Portell (Castellón) – Spain
Torre Julian	Lower Cretaceous (Aptian)	Dinosaur	Todolella (Castellón) – Spain
Peguera 1-Figols	Upper Cretaceous	Dinosaur (Hadrosauria)	Figols (Barcelona) – Spain
Serrat-C	Upper Cretaceous	Dinosaur (Hadrosauria)	Abella de la Conca (Lleida) – Spain
Molì	Upper Cretaceous	Dinosaur	Isona (Lleida) – Spain
La Llau	Upper Cretaceous	Dinosaur	Abella de la Conca (Lleida) – Spain
Nerets	Upper Cretaceous	Dinosaur	Vilamitjana (Lleida) – Spain
Pous	Upper Cretaceous	Dinosaur	Basturs (Lleida) – Spain
Serrat-R2	Upper Cretaceous	Dinosaur	Abella de la Conca (Lleida) – Spain
Basturs Poble	Upper Cretaceous (Maastrichtian)	Dinosaur (Titanosauria)	Basturs (Lleida) – Spain
La Boixedat	Eocene (lower Lutetian)	Reptile (Crocodryle)	Huesca – Spain
La Boixedat	Eocene (lower Lutetian)	Turtle plate (Neochelys)	Huesca – Spain
Ulldemolins	Eocene (lower Lutetian)	Undetermined mammalian	Ulldemolins (Tarragona) – Spain
Sossis	Eocene (Bartonian)	Undetermined bone fragment	Sossis (Conca de Dalt) (Lleida) – Spain
Sant Cugat De Gavadons	Eocene (Priabonian)	Undetermined bone fragment	Sant Cugat de Gavadons (Barcelona) – Spain
Roc De Santa II	Eocene (Priabonian)	Undetermined reptile	Roc de Santa (Conca de Dalt) (Lleida) – Spain
La Costa Blanca	Lower Miocene (21 Ma)	Turtle plate	La Costa Blanca (Castellbisbal) (Barcelona) – Spain
Els Casots	Lower Miocene (15.5–16 Ma)	Undetermined bone fragment	Subirats (Barcelona) – Spain
Punt De Prosp.1	Upper Miocene (13 Ma)	Undetermined bone fragment	Hostalets de Pierola (Barcelona) – Spain
Trinxera De Sant Quirze	Middle Miocene (13–11 Ma)	Undetermined mammalian	Sant Quirze (Barcelona) – Spain
Punt De Prosp.13	Upper Miocene (10.5 Ma)	Turtle plate	Hostalets de Pierola (Barcelona) – Spain
Edar	Upper Miocene (10–9 Ma)	Undetermined bone fragment	Sabadell (Barcelona) – Spain
Concud	Upper Miocene (7.1–8.2 Ma)	Turtle plate	Concud (Teruel) – Spain
Crespià	Lower Pliocene	Rhinoceros (*Stephanorhinus etruscus* sp.)	Crespià (Girona) – Spain
Cal Guardiola	Lower Pleistocene (900.000 years)	Proboscidea	Terrasa (Barcelona) – Spain
Cal Guardiola (Mamut)	Lower Pleistocene	Mammoth (*Archidiskodon meridionalis* sp.)	Terrasa (Barcelona) – Spain
Barranco Leon	Lower Pleistocene	Undetermined bone fragment	Orce (Granada) – Spain
Atapuerca	Lower Pleistocene	Mammalian (Perissodactila)	Ibeas de Juarros (Burgos) – Spain
La Boella	Lower Pleistocene	Undetermined bone fragment	La Canonja (Tarragona) – Spain
Avenc Del Marcel	Lower Pleistocene	Undetermined bone fragment	Vallirana (Barcelona) – Spain
Cova Matutano	Middle Pleistocene	Undetermined bone fragment	Vilafamès (Castelló) – Spain
Castelldefels	Middle Pleistocene	Turtle plate	Castelldefels (Barcelona) – Spain
Tossal De La Font	Upper Pleistocene	Undetermined bone fragment	Vilafamès (Castelló) – Spain
Cueva Del Cortadillo	Upper Pleistocene	Undetermined bone fragment	Castelló – Spain
Aveiros da Cima	Upper Pleistocene	Undetermined bone fragment	Portugal
Cova Mollet	Upper Pleistocene	Undetermined mammalian	Serinyà (Girona) – Spain
Serinyà	Upper Pleistocene	Undetermined mammalian	Serinyà (Girona) – Spain
Serinyà 1C	Upper Pleistocene	Undetermined mammalian	Serinyà (Girona) – Spain
Son Olivaret	Holocene (III millennium B.C.)	*Homo sapiens*	Menorca – Spain
Necropolis De Ripollet	Holocene (Neolitic)	*Homo sapiens*	Ripollet (Barcelona) – Spain
Prolagus sardus	Holocene (Neolitic)	Mammalian (*Prolagus sardus* sp.)	Ossi (Sassari) – Italy
Monte Sirai T9	Holocene (IV century B.C.)	*Homo sapiens*	Sant'Antioco (Carbonia) – Italy
Rhesus Monkey	Holocene (2007 A.D.)	*Rhesus Monkey*	University of Teeside (Middlesbrough) – UK

about 2 cm. A Si-PIN detector from AMPTEK was employed with a thickness of about 300 μm and characterized by an energy resolution of about 200 eV at 5.9 keV.

It is remarked that while XRF supplies the elemental composition of osseous materials, the powder diffraction technique inspects the phase constitution. Moreover, for any phase evaluated from the patterns, the geometry and structure lattice parameters are assessed, together with microstructure parameters like crystallite size and lattice strain.

3. Results and discussion

We start our data analysis first by comparing the XRD and XRF analyses in samples representative of limiting cases. Such cases concern single-phase palaeontology bones as well as multiphasic bones with unusual phase and elemental constitution. In addition to this, we have thought it useful to evaluate the XRD and XRF features of the oldest fossil of our collection, which may be remarkable since older than previous fossils studied by XRD in the literature. Crystallite size homogeneity will be discussed in relation to samples from the same geological setting. Later, the whole quantitative information acquired will be discussed.

3.1. Comparison between XRD and XRF data

Fig. 1 (lhs) shows the XRD patterns of *Rhesus Monkey*, *Cal Guardiola Mamut* and *Patiras* specimens. The experimental data points of all specimens are well described entirely with the structure factor of monoclinic hydroxylapatite biomineral, suggesting that these bones are actually single-phase even if they remained buried for very different periods. Note that the normalized cell volume reported in Table 2 for the specimen *Patiras* is smaller than the value for biogenic apatite, suggesting the progression of a fluoritisation mechanism. In addition, the average crystallite size of *Patiras* specimen, determined from the line broadening analysis incorporated in the Rietveld refinement, gives a figure of 420 Å, definitely larger than the value of 252 Å for *Cal Guardiola Mamut* and also larger than the value of 170 Å determined in modern or ancient human bones using the same methodology (Piga et al., 2008b). We note also that this increase of crystallite size is in qualitative agreement with that obtained by Elorza et al. (1999) who used a crystallinity index of dinosaur bones in terms of half width at half maximum of the (002) peak.

The typical XRF spectrum collected for the same specimens is reported in Fig. 1 (rhs), which in turn closely resembles the pattern reported for a dinosaur bone by PIXE analysis (Goodwin et al., 2007). This is not surprising, because both techniques collect the X-ray emission of elements stimulated by an X-ray beam in the former case and by particles (protons or electrons) in the latter. The peak at 2 keV was attributed to phosphorous, while that at ca 3 keV is due to Argon. The strong doublet at energies of 3.7 and 4.0 keV respectively is attributable to the α and β emission lines of the calcium element. Obviously the calcium and phosphorus elements derive from the HA biomineral of bones. The shoulder at ca 3.3 keV may be attributed to potassium. Also, the doublets at ca 6.4 and 7.1 keV respectively, which are missing in the *Rhesus Monkey* spectrum, are due to α and β lines of iron, while the peak at ca 8 keV is attributed to the α line of copper.

In addition to this, the presence of the strontium element can be surmised from the peaks at 14.0 and 15.8 keV respectively. Weak traces of chromium, manganese, rubidium, yttrium, zirconium, niobium and molybdenum elements can also be suspected from the minor peaks although the latter element may be an artifact due to the source used.

It is possible to ascribe such presence of minor elements at varying degree of intensity, at least partially, to the taphonomic and diagenetic process evolution to which the bones have been involved. However, as the comparison with *Rhesus Monkey* suggests, some trace elements like Zr, Nb and Mo may be accumulated in the bones during the life cycle of the animal species. In any case, given the single-phase nature of this specimen assessed by XRD, it may be conjectured that these ions replace those of calcium in the apatite lattice. Of course also monovalent K cations, suspected from the shoulder of the main peak of Ca, may be involved in this substitution.

The combined XRD–XRF inspection of the *Qurolles-M* specimen supplies new appealing aspects.

The XRD pattern refinement reported in Fig. 2 (lhs) shows that the bone specimen is not anymore single-phase. As reported in the Table 2, the apatite-like phase is the most abundant, but is accompanied by ca 25 wt% of goethite and small quantities of calcite and quartz. Note also that the average crystallite size of the "apatitic" phase is 349 Å and the pseudo-hexagonal cell volume of 521.9 $Å^3$, that is very similar to the fluorapatite.

IThe XRF spectrum in Fig. 2 (rhs) displays a strong contribution from iron which appears even more intense than calcium. Note also weak traces of transitional elements such as Y, Sr, Ti, Cr, Mn, Zn and Pb. The presence of goethite was also reported (Elorza et al., 1999) though not evaluated quantitatively, and was attributed to a hydromorphic process because of seasonal variations of the phreatic water

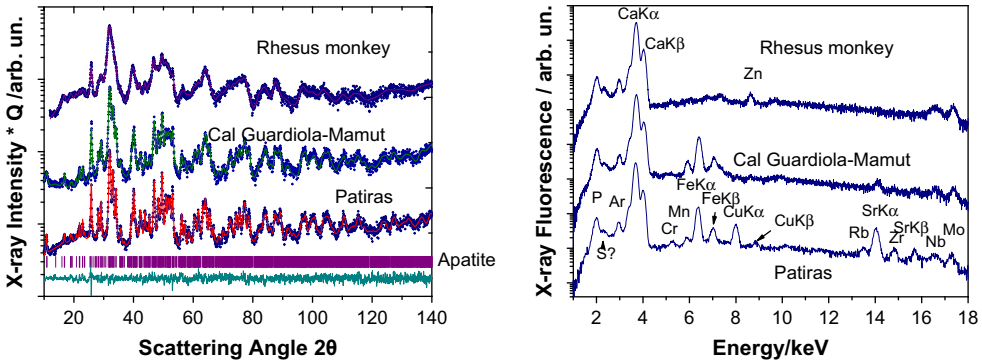

Fig. 1. Lhs) The XRD patterns (data points) and Rietveld fit (full line) of *Rhesus Monkey*, *Cal Guardiola Mamut* and *Patiras* samples assess the single-phase condition of the bone specimens which have been subjected to different regimes of burial. It can be surmised that the phase condition alone is not sufficient for a satisfactory description of diagenetic effects. A peak sharpening is evident from top to bottom. The sequence of bars mark the peak positions expected from the structure factor of monoclinic apatite, while the data scattering at the bottom refer to the residuals after the fit of Patiras specimen. (Rhs) The XRF spectra of the same specimens showing line contributions from P, Ca, Fe, Cu, Sr elements together with other transitional elements in trace, such as Cr, Mn, Zn, Rb, Y, Zr, Nb, Mo. The peak of Ar is attributed to air.

Table 2
List of structure and microstructure parameters of hydroxylapatite structure from phases' analysis by XRD and the associated estimated standard deviation.

Sample	Phase (%)	Average crystallite size (Å) (±5%)	a/Å (±0.001)	b/Å (±0.002)	c/Å (±0.001)	γ/° (±0.05)	$V_c/2$/Å^3 (±0.3)
Menorca IPS35594	Apatite 48% Calcite 35% Quarzo 5% Dolomite 11% Kaolinite < 1%	802	9.380	18.735	6.894	120.22	523.43
La Mora	Apatite 52% Calcite 35% Quarzo 9% Dolomite 6%	727	9.381	18.742	6.893	120.24	523.50
Menorca IPS37436	Apatite 64% Calcite14% Dolomite 18% Quarzo 3% Kaolinite 1%	611	9.372	18.692	6.892	119.96	523.01
Losilla	Apatite 40% Calcite 33% Quarzo 19% Kaolinite 8%	592	9.347	18.778	6.894	120.15	523.16
Aras De Alpuente	Apatite 58% Calcite 42%	554	9.354	18.711	6.901	119.75	524.32
La Ventura	Apatite 62% Calcite 29% Quarzo 9%	453	9.344	18.766	6.900	120.02	523.80
El Collado	Apatite 75% Calcite 25%	522	9.340	18.711	6.905	119.78	523.68
Patiras	Apatite 100%	420	9.3481	18.796	6.897	120.12	524.11
CL42	Apatite 26% Calcite 72% Quarzo 2%	576	9.362	18.742	6.899	119.94	524.49
La Fita	Apatite 72% Calcite 28% Quarzo 1%	415	9.393	18.763	6.903	120.29	525.25
La Cuba	Apatite 80% Calcite 19% Quarzo 1%	398	9.344	18.750	6.903	119.96	523.90
SAV67	Apatite 85% Quarzo 7% Berlinite 1% Caolinite 7%	457	9.363	18.817	6.897	120.16	525.32
Povet	Apatite 67% Kaolinite 25% Quarzo 8%	437	9.372	18.735	6.899	120.10	524.00
Comptadors_A1	Apatite 66% Calcite 24% Quarzo 8% Caolinite 2%	432	9.365	18.822	6.896	120.13	525.66
Todolella_1	Apatite 98% Calcite 1% Quarzo 1%	436	9.365	18.823	6.894	120.16	525.37
Camino	Apatite 80% Calcite 20%	2107	9.377	18.748	6.894	120.02	524.69
EAP 40-39	Apatite 93% Calcite 3% Quarzo 3% Goethite 1%	485	9.345	18.796	6.894	120.00	524.34
Qurolles-M	Apatite 84% Dolomite 15% traces of $SiO_2 + CaCO_3$	383	9.366	18.702	6.895	120.20	521.09
MC1–5	Apatite 85% Calcite 15% Quarzo (tracce)	411	9.351	18.772	6.893	120.18	522.98

(*continued on next page*)

Table 2 (*continued*)

Sample	Phase (%)	Average crystallite size (Å) (±5%)	a/Å (±0.001)	b/Å (±0.002)	c/Å (±0.001)	γ/° (±0.05)	$V_c/2$/Å^3 (±0.3)
Torre Julian	Apatite 52% Calcite 47% Quarzo 1%	411	9.340	18.738	6.901	119.75	524.30
Peguera 1-Figols	Apatite 74% Calcite 14% Quarzo 7% Kaolinite 5%	600	9.344	18.799	6.890	119.99	524.12
Serrat-C	Apatite 55% Calcite 44% Quarzo 1%	575	9.342	18.759	6.897	119.90	523.90
Molì	Apatite 48% Calcite 15% Quarzo 8% Celestite 25% Kaolinite 4%	740	9.310	18.774	6.902	120.11	521.79
La Llau	Apatite 81% Calcite 12% Goehite 7%	559	9.362	18.705	6.897	119.81	523.98
Nerets	Apatite 80% Calcite 19% Quarzo 1%	581	9.344	18.771	6.900	120.01	523.99
Pous	Apatite 59% Calcite 37% Quarzo 4%	449	9.361	18.674	6.899	119.82	523.16
Serrat-R2	Apatite 36% Calcite 59% Quarzo 5%	633	9.358	18.711	6.897	120.03	522.77
Basturs Poble	Apatite 55% Calcite 35% Quarzo 10%	612	9.333	18.759	6.900	119.99	523.18
La Boixedat crocodryle	Apatite 56% Calcite 34% Quarzo 10%	357	9.355	18.775	6.90	120.28	523.29
La Boixedat turtle	Apatite 36% Calcite 64%	409	9.304	18.724	6.901	119.67	522.29
Ulldemolins	Apatite 73% Calcite 24% Quarzo 2%	336	9.336	18.656	6.894	119.68	521.61
Sossis	Apatite 70% Calcite 24% Quarzo 4% Kaolinite 2%	241	9.327	18.893	6.90	120	526.49
Sant Cugat De Gavadons	Apatite 77% Calcite 19% Quarzo 4% Kaolinite tracce	342	9.323	18.747	6.903	119.71	523.95
Roc De Santa II	Apatite 60% Calcite 31% Quarzo 9% Kaolinite tracce	291	9.345	18.792	6.903	120.24	523.64
La Costa Blanca	Apatite 63% Calcite 35% Quarzo 2%	405	9.358	18.795	6.893	120.30	523.38
Els Casots	Apatite 58% Calcite 42%	281	9.336	18.704	6.911	119.58	524.76
Trinxera De Sant Quirze	Apatite 65% Calcite 26% Quarzo 9%	304	9.334	18.802	6.90	119.97	524.51
Punt De Prosp.13	Apatite 60% Calcite 36% Quarzo 4%	250	9.398	18.774	6.899	120.44	524.73

Table 2 (*continued*)

Sample	Phase (%)	Average crystallite size (Å) (±5%)	a/Å (±0.001)	b/Å (±0.002)	c/Å (±0.001)	γ/° (±0.05)	$V_c/2$/Å^3 (±0.3)
Punt De Prosp.1	Apatite 75% Calcite 21% Quarzo 4%	272	9.342	18.822	6.906	119.95	526.08
Edar	Apatite 100%	252	9.327	18.772	6.905	119.77	524.71
Concud	Apatite 91% Calcite 9%	203	9.357	18.854	6.906	120.60	524.34
Crespià	Apatite 98%	248	9.399	18.722	6.903	120.28	524.49
Cal Guardiola	Apatite 99% Quarzo 1%	208	9.36	18.815	6.90	120.30	526.02
Cal Guardiola Mamut	Apatite 100%	252	9.374	18.813	6.897	120.35	524.81
Barranco Leon	Apatite 79% Calcite 7% Quarzo 14%	184	9.391	18.780	6.90	120.39	524.85
Atapuerca	Apatite 79% Calcite 20% Quarzo 1%	190	9.427	18.791	6.893	119.76	530.00
La Boella	Apatite 98% Calcite 2%	217	9.394	18.836	6.898	119.97	528.68
Avenc Del Marcel	Apatite 95% Calcite 3% Quarzo 2%	280	9.385	18.867	6.894	120.19	527.56
Cueva Matutano	Apatite 98% Calcite 2%	197	9.388	18.898	6.896	120.20	528.70
Castelldefels	Apatite 42% Calcite 58%	280	9.336	18.704	6.911	119.58	524.76
Tossal De La Font	Apatite 73% Calcite 26% Quarzo 13%	194	9.374	18.886	6.889	119.94	528.43
Cueva Del Cortadillo	Apatite 95% Calcite 5%	249	9.370	18.866	6.892	120	527.55
Aveiros da Cima	Apatite 39% Calcite 49% Quarzo 5% Barite 7%	262	9.418	18.678	6.892	119.86	525.71
Cova Mollet	Apatite 37% Calcite 63%	211	9.402	18.817	6.901	120.38	526.63
Serinyà	Apatite 100%	178	9.360	18.834	6.902	120.07	526.49
Serinyà 1C	Apatite 97% Calcite 3%	260	9.370	18.724	6.893	119.54	526.07
Son Olivaret	Apatite 97% Quarzo 3%	168	9.458	18.810	6.891	119.65	532.61
Necropolis De Ripollet	Apatite 87% Calcite 13%	176	9.464	18.820	6.888	120.10	530.70
Prolagus sardus	Apatite 85% Calcite 13% Quarzo 25%	168	9.440	18.898	6.896	120.67	529.07
Monte Sirai T9	Apatite 98% Calcite 2%	169	9.407	18.854	6.899	119.70	531.43
Rhesus Monkey	Apatite 100%	169	9.37	18.820	6.902	119.09	531.80

level. In any case, the presence of a considerable fraction of goethite from XRD is in good agreement with the high level of iron from XRF.

The specimen *Aveiros da Cima* (bottom pattern of Fig. 2 at the lhs) shows a phase constitution similar to *Qurolles-M* except for the goethite phase, which is here substituted by barite. This is sufficient to change sensibly the profile of elements extracted from the correspondent XRF spectrum (Fig. 2, bottom trace at the rhs), where we can recognize barium and titanium elements at an appreciable level of concentration. Of course, the presence of barium has to be related to barite while titanium may substitute for calcium in apatite, given the absence of any Ti-based phase in this sample.

The combined XRD and XRF analysis conducted on the *La Llau* specimen proposes a more direct interpretation.

The XRD pattern reported in Fig. 3 (lhs) shows that the specimen is made up of three phases, namely an "authigenic apatite" component with unit cell volume of 524.0 Å^3 which is again identifiable as a fluorapatite, accompanied by the calcite and goethite phases. In addition, an average crystallite size of 559 Å was

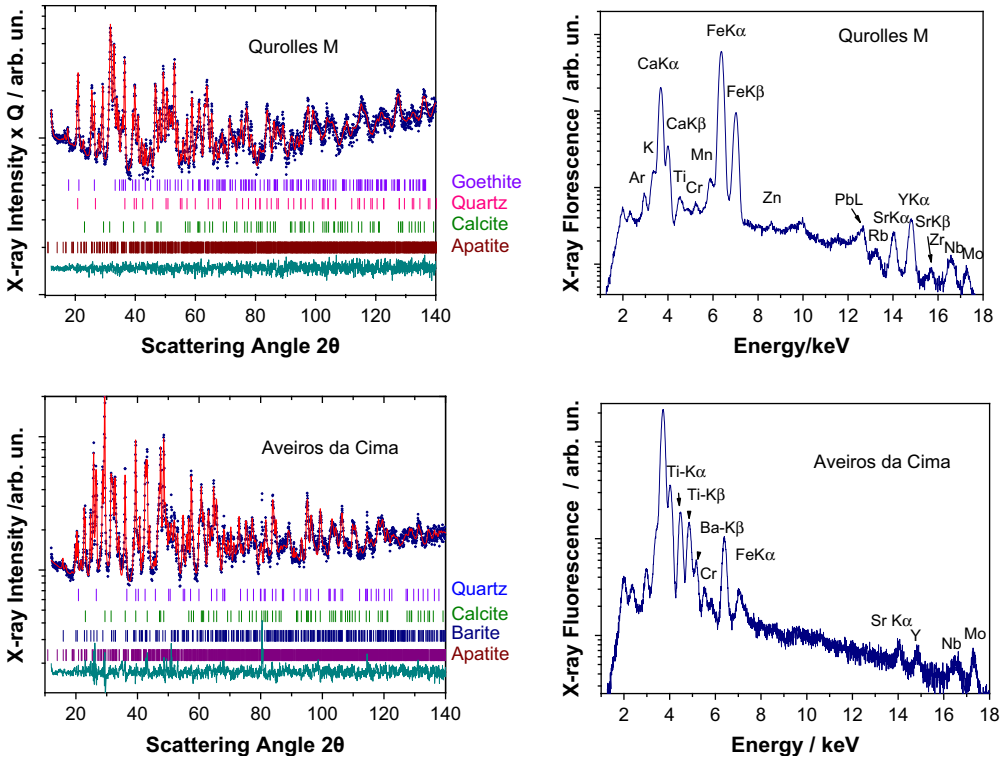

Fig. 2. (Lhs) The XRD pattern (data points) and Rietveld fit (full line) for the *Qurolles-M* specimen points out the consistent presence of goethite FeOOH. The specimen *Aveiros da Cima* is again a mixture of four phases but goethite is replaced by barite. The bottom line refers to the residuals, while the sequence of bars mark the peak positions expected for each phase indicated at the rhs of the pattern. (Rhs) The XRF spectra of the same specimens show a contribution from the Fe element even stronger than that of Ca in the *Qurolles-M* specimen, while in *Aveiros da Cima* the iron contribution is much weaker and comparable to that of titanium. Note also the presence of other transitional elements in trace.

retrieved from the line broadening analysis incorporated in the Rietveld fit. As it can be seen in Fig. 3 (rhs) the main lines are from calcium, phosphorous, strontium and iron elements, while weak lines are also present for the minor elements such as sulphur, potassium, titanium, manganese, rubidium, yttrium and possibly arsenic. Thus, it can be surmised that the presence of iron from the XRF lines is coming from the goethite phase, which is 7% wt in the sample. In addition, strontium and the minor elements found are likely to substitute for Ca in the fluorapatite structure.

To pursue further the comparison, we report in Fig. 4 (lhs) the XRD pattern of the *Molì* specimen showing new and complex phase distribution. Beyond the "authigenic apatite" phase, which is ca 48% wt of the specimen, this time we have assessed the presence of the celestite ($SrSO_4$) phase at a 25% wt level, accompanied by calcite, quartz and ca 4 wt% of kaolinite. In fact, the cell volume of the "apatitic" phase turns out again close to that of fluorapatite. With respect to the previous XRD patterns it is also possible to evaluate a peak sharpening on account of an increased crystallite size which turns out to be extended on average 740 Å. In accordance, the XRF spectrum shows a different profile of the element distribution. The presence of Fe emission lines is particularly evident together with those of Sr. There are also minor quantities of Ti, V, Cr, Mn, Cu, Zn, As and perhaps Ga. Note also the absence of a significant contribution from yttrium and Nb atoms. The relatively strong intensity of Fe α and β emission lines deserves a further explanation. In spite of the five phases resolved by the XRD approach, none of them correspond to common oxide–hydroxides Fe-based phases like goethite, hematite, etc. Then, the consistent presence of Fe may be justified with a substitution of calcium atoms by iron in the apatite structure and/or a similar substitution in the

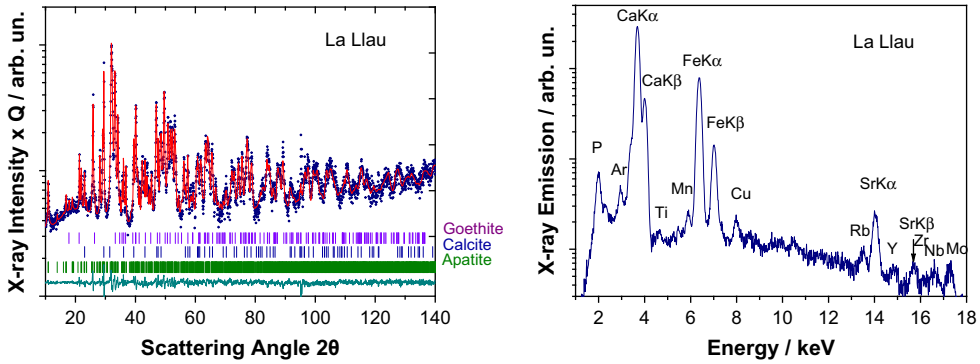

Fig. 3. (Lhs) The XRD pattern of *La Llau* specimen (data points) and its fit according to Rietveld (full line) points to the presence of 7 wt% of the goethite phase in addition to the expected presence of fluorapatite and calcite. (Rhs) The XRF spectrum shows again an important contribution of the FeKα and β lines but the contribution of the Sr lines appears less important than in the case of *Molì* specimen.

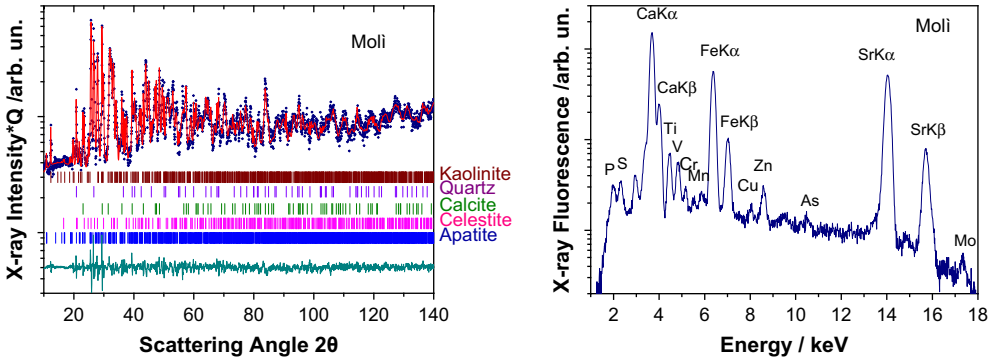

Fig. 4. (Lhs) The XRD pattern of *Molì* specimen shows a rather complex phase constitution of five phases, with the notable presence of the celestite structure $SrSO_4$. (Rhs) The XRF spectrum shows intense line profiles from Ca, Fe and Sr elements accompanied by weak lines from P, S, Ar, Ti, V, Cr, Mn, Cu, Zn, As and Mo elements.

kaolinite phase by iron for aluminium. Note that no example of dinosaur bones with important contribution by celestite phase by XRD is reported in the literature.

We close this comparison session with the *Menorca IPS35594* specimen which is the oldest in our collection (Middle Triassic, ca 245 Ma). From Fig. 5 it can be seen that this sample is constituted by a mixture of five phases, with some difference with respect to the *Molì* specimen in that the celestite phase is replaced by the dolomite. Accordingly, its XRF spectrum does not show appreciable presence of strontium. Conversely, the presence of relatively intense iron doublet, not mirrored by an iron-based phase in the XRD pattern suggests again the iron is incorporated as vicariant element in the lattices of apatite or kaolinite phases. Note also the large value obtained for the average crystallite size.

Another important issue concerns the phase and chemical homogeneity of bone pieces extracted from the same geological area for which we propose to compare the XRD pattern of specimens *Camino* and *EAP 40-39*.

As it can be seen in Fig. 6, just the "apatitic" and calcite phases are present in both specimens, though to a different fraction level.

There is an evident difference in the peak broadening of the two patterns, on account of average particle size of 2100 Å and 382 Å for the *Camino* and *EAP 40-39* specimens, respectively. This huge difference of the average crystal size values suggests that correlation between crystallization indexes and bone age has to be regarded with obvious caution.

3.2. Quantitative mineralogical phases in bones and diagenesis

According to the data summarized Table 2, the most frequent phases found in the samples studied by XRD are apatite, calcite and quartz. It is clear even from the previous presentation of patterns that there is no correlation between the amount of a specific phase and the bone fossil age. In fact, we may notice that the apatite phase may be present in the bones here examined from 100% (*Rhesus Monkey*, *Serinyà*, *Cal Guardiola Mamut*, *Edar*, *Patiras*) to only 26 wt% in the case of specimen *CL42*, where, conversely, the maximum percentage amount of calcite 72 wt% occurs.

A maximum amount of 7–8.0 wt% biogenic calcite is possible to occur in human bones (Wopenka and Pasteris, 2005). The precipitation of calcite as an authigenic mineral is common in most fossil sites (Hubert et al., 1996; Astibia et al., 2005). Less frequently, calcite is observed also as a millimetric white crust between bone and crust.

As for quartz mineral, generally it does not exceed 14 wt% in our collection, apart from two exceptions in *Prolagus Sardus* (25 wt%) and *Losilla* (19 wt%). Quartz normally derives from sediments, but rarely is an authigenic mineral.

In the other specimens here investigated we have also evaluated other phases such as dolomite [$CaMg(CO_3)_2$], goethite (FeOOH), kaolinite [$Al_2Si_2O_5(OH)_4$], celestite ($SrSO_4$), barite ($BaSO_4$) and berlinite ($AlPO_4$) at varying level of fractions. In any case, mineralogical and compositional changes in bones exposed (forty years maximum) on soil surface, were recently reported using thin section petrography (Trueman et al., 2004).

Particularly, cations introduced into the bone/water system during passage of pore waters may be either adsorbed onto exposed bone crystallites, or incorporated into authigenic minerals. Thus, evaporation at the ground surface may induce infiltration of water in bones leading to the presence of barite. Concerning celestite, our finding appears new within the literature of diagenesis of bones. It was reported (Rushdi et al., 2000) that both barite and celestite coexist in the marine environment with significant fractions of Sr and Ba in solid solution. In the marine environment celestite is primarily found as the skeletal component of the marine planktonic

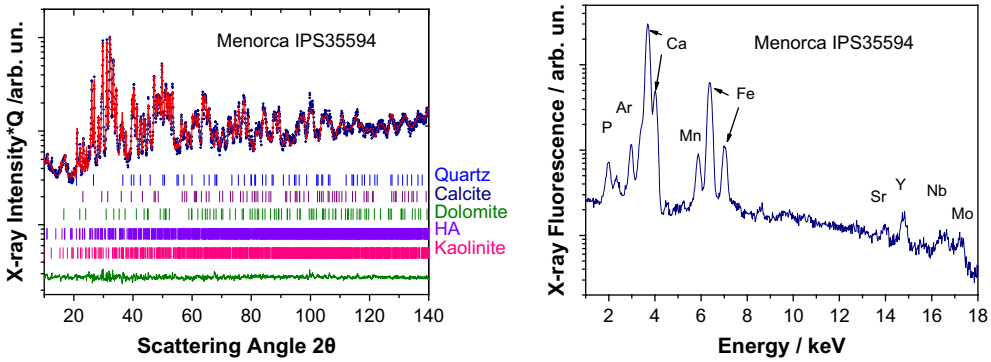

Fig. 5. XRD–XRF comparison for the *Menorca IPS35594* specimen, the oldest of our collection. While the XRF spectrum at the rhs shows a rather conventional aspect with the presence of Ca and Fe elements, the XRD pattern highlights a complex phase constitution, with the absence of iron-based phases. This suggests that iron element is incorporated as vicariant in other phases, likely apatite or kaolinite.

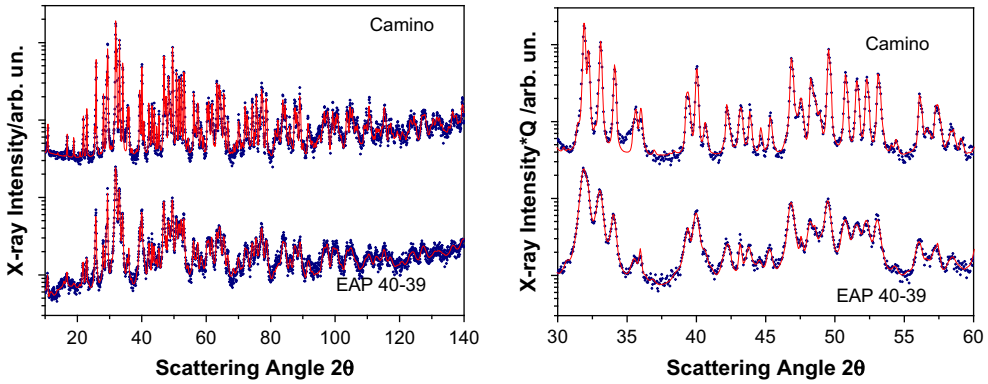

Fig. 6. (Lhs) The XRD patterns of two bones from different dinosaurs sampled in the same geological area. The upper pattern referred to the *Camino* specimen shows sharp line profiles from the fluorapatite with respect to the *EAP 40-39* specimen at the bottom, on account of markedly different average crystallite size. (Rhs) This comparison may be better evaluated across a narrower angular range.

organism acantharian, but we can hardly establish some correlation among barite, celestite and a possible marine environment in our bones. The provenance of these phases and elements from hydrothermal environments appears more likely at this stage of the study.

Quartz and goethite phases were also found in dinosaur and other bones belonging to the Upper Cretaceous (Elorza et al., 1999). Nonetheless, we did not find traces of siderite $FeCO_3$ which instead was observed on a collection of fossil bones by Wings (2004) and Farlow and Argast (2006). The clay matrix studied by Elorza et al. (1999) showed presence of kaolinite and illite phases, so it is possible that the kaolinite in our specimens derives from infiltration of the clay mineral. Dolomite is reported less frequently, and in one case is referred to as magnesium calcite (Wings, 2004). We remind that with XRD the evaluation of space group and lattice parameter of the magnesium–calcium carbonate phase enables to distinguish "stoichiometric" dolomite from a magnesium calcite solid solution or huntite (Dollase and Reeder, 1986).

The refined values of lattice parameters of the monoclinic cell have been divided by two to give a pseudo-hexagonal cell value $V_M/2$ to make a comparison with the data from literature. These values change from an upper figure of 532.80 Å^3 (*Rhesus Monkey*) to a lower volume of 521.61 Å^3 (specimen *Ulldemolins*). The upper value estimated in this work for sample *Rhesus Monkey* is in keeping with the volume determined in biogenic phases without fluorine substitution (Hughes et al., 1989). Note that the literature data referred to fluorapatite, that is, authigenic apatite, supply several unit cell volume values ranging from 522.18 Å^3 to 528.41 Å^3, respectively (Sudarsanan et al., 1972; Sudarsanan and Young, 1978). Also, for the francolite authigenic phase, the literature values go from a minimum of 518.73 Å^3 to a maximum of 523.81 Å (Perdikatsis, 1991; Elorza et al., 1999). So, the volume of the cells of older specimens is generally close to the values reported in the literature for fluorapatite and francolite (McConnell, 1973; Hughes et al., 1989). The unit cell volume data reported in Fig. 7 scatter around an exponential-like function of the time t:

$$V_C = V_F + (V_{HA} - V_F)\, e^{(-kt)}$$

In fact, from the fit of patterns of Fig. 1 we have determined that the normalized unit cell volume of *Rhesus Monkey* "modern" bone is $V_{HA} = 532\ (\pm 0.3)$ Å^3 and the cell volume V_C of fossils decreases down to values of fluorapatite $V_F = 523\ (\pm 0.3)$ Å^3 after a decay time $1/k = (4\text{–}5\ \text{Ma})^{-1}$. This reduction process of unit cell volume is attributed in the literature to a biogenic–authigenic post-mortem transformation and mainly consists in a fluoritisation, i.e., the replacement of –OH groups by fluorine atoms. In summary, the unit cell volume from XRD data may be used to give an overall account for the mineralization processes undergone by the apatite phase as it was recently suggested by Stathopoulou et al. (2008). Of course our data do not refer to the bone situation studied by Trueman et al. (2004).

This is indirectly confirmed by our recent studies on various archaeological cremated human bones, where we have assessed that cremation and incineration rituals make the average crystallite size value of HA to increase, but the unit cell volume remains essentially unchanged (see Table 3).

Also, in Fig. 7, the unit cell values referred to times longer than 5 Ma may deviate from the fluorapatite value of 520 Å^3 due to exchange of ionic species other than fluorine. In any case this permits, after a combined analysis of the unit cell volume and the average crystallite size values, to conjecture more consciously about the age of a fossil bone. In fact, our analysis shows that specimens that have average crystallite size larger than 300 Å simultaneous to unit cell volumes lower than 525 Å^3, may be older than 5 Ma. The bone specimens with average crystallite size values up to 800 Å may be as old as 220 Ma. This may be used as a rule-of-thumb to infer the age of very old fossils in the absence of other more stringent indications. This analysis confirms once more that that it is very difficult to assess objectively the age of bone fossils using XRD alone but valuable information content

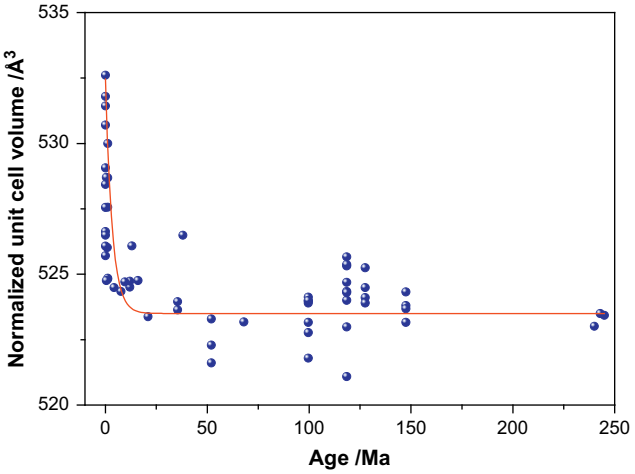

Fig. 7. The behaviour of the pseudo-hexagonal cell volume of apatite phase (calculated as in the text) as a function of the bone fossil age determined according to stratigraphic methods. The change in the cell volume following an exponential decay reflects the biogenic-to-authigenic transformation of bone apatite due to a fluoritisation process and seems to be accomplished after 4–5 Ma.

Table 3
Average crystallite size, lattice parameter values and reduced unit cell volume of eight Spanish and Italian incinerated bones. For this relatively modern period of these bones one sees that the unit cell volume remains essentially unchanged vs the high degree of thermal treatment, as testified from the high values of average crystallite size found by XRD.

Sample	Site of provenance	Chronology	Average cristallize size (Å)	a/Å	b/Å	c/Å	γ/°	$V_c/2/Å^3$
C3G13T1	Aguilar de Montuenga (Soria, Spain)	IV–III century B.C.	3507	9.420	18.856	6.895	120.01	530.26
C4T5	Aguilar de Montuenga (Soria, Spain)	IV–III century B.C.	2934	9.439	18.861	6.884	119.92	531.11
T250	Monte Sirai (Carbonia, Italy)	VI century B.C.	2316	9.421	18.841	6.889	119.99	529.54
C5T10-1	Aguilar de Montuenga (Soria, Spain)	IV–III century B.C.	1890	9.417	18.848	6.886	119.97	529.39
T252	Monte Sirai (Carbonia, Italy)	VI century B.C.	1724	9.426	18.858	6.892	120.01	530.43
SR96	Son Real (Mallorca, Spain)	VI–II century B.C.	1499	9.425	18.840	6.884	120	529.30
SP13-UE10050	Necropolis de Sebès (Tarragona, Spain)	VII–VI century B.C.	1144	9.420	18.828	6.887	120.01	528.86
IPA9	S'Illot des Porros (Mallorca, Spain)	VI–II century B.C.	957	9.413	18.842	6.889	119.95	529.33

concerning the mineralization processes is in any case available from the X-ray patterns.

In any case, this correlation is presented in Fig. 7 after considering all the average crystallite size values from Table 2, where the correspondent age values are from the periods estimated after stratigraphic analyses. The figure of specimen *Camino* was considered an outlier and excluded from the following analysis.

It is important to note that a plot of the normalized unit cell volume as a function of age, reported in Fig. 7, shows a different trend that can be useful to discriminate the specimens, that is, specimens with cell volume V_C close to that of HA are certainly recent (younger than 2–3 Ma) while those that appears fluorinated are certainly older. A rough estimate of the age from average crystallite size can be tried.

Several objections may be raised to the specimen collection here examined, particularly for what it concerns its distribution across the variable age. One point may concern the reliability of the assumption involved in the XRD technique to evaluate with enough precision the average crystallite size value. Further, we note that the wide data scatter above the straight line of Upper Cretaceous specimens (evidenced in Fig. 8) may suggest that, beyond the uncertainties due to the technique itself, other local effects may bias the crystallite growth according to specific conditions of burial.

In any case, it can be seen that the data roughly conform to a linear trend as a function of age. The estimated intercept value at 0 time is 222 (±30) Å, which agrees only partially with the average crystallite size of 168 (±8) Å determined in modern monkey bones (*Rhesus Monkey*). The results and conclusions appear obviously different from those reported by Person et al. (1995, 1996), but also from those by Bartsiokas and Middleton (1992), where a linear trend was envisaged as a function of the logarithm of age. The linear trend here observed suggests that the increase of average crystallite size vs diagenesis may be associated to a zero-order kinetics process.

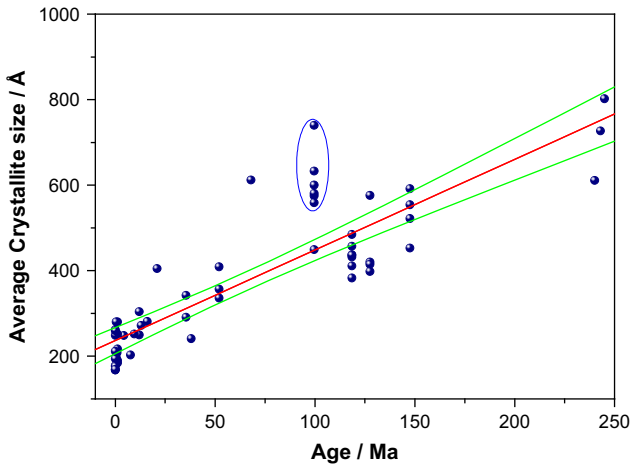

Fig. 8. Correlation between average crystallite size values and age from stratigraphic chart analysis of the bony specimens here analysed. The data inside the ellipse refer to specimens from Upper Cretaceous not conforming to the linear trend. The confidence band at 95% is also shown.

4. Conclusions

Diagenetic changes are induced in bones over palaeontologist times mainly by complex mineralogical and physico-chemical processes. The investigations and analyses by XRD and XRF here reported supplied detailed and to a certain extent satisfactory accounts of the post-mortem integral changes to which the bones have been subjected. However, the whole of these changes observed in 61 bones of various ages from present to ca 245 Ma may be spatially and temporally discontinuous because of several factors which are difficult to assess unambiguously. In fact, the mineralization processes are considerably affected by the soil chemistry, which in turn may be determined by the local conditions of burial. This may be different with respect to the life environment typical of the specific animal species to which the fossil belongs. As it concerns the HA phase, this seems always subjected to a fluoritisation mechanism, i.e., the –OH hydroxyl group is replaced by F with some continuity, as it emerges from the variations of the unit cell volume as a function of the age. In the specimens here examined, the process seems to be accomplished after 4–5 Ma according to a simple kinetic equation of first-order.

The most frequent minerals accompanying the HA of bones were found to be calcite and quartz. Also, goethite was frequently observed as additional phase. In fact, the XRF data points out that iron is the most frequent element encountered in bone material after the obvious presence of calcium and phosphorous. Less frequently kaolinite was also observed. The phase analysis by XRD has also pointed out to the sporadic occurrence of sulphate phases, e.g., barite and celestite even if separately. It is clear that the presence of these minerals may affect heavily the diagenetic processes but there is no way to relate the presence of specific phases with a peculiar effect or to predict its contribution to ageing. Under these circumstances we have found a sensible correlation between the average crystallite size of HA and the age of the specimens, confirming the very slow growth of coherent domains of diffraction vs annealing times at the burial temperature of the setting.

The correlation found appears realistically rough because of several methodological uncertainties. Two of them are particularly important in our opinion. First, assuming that the growth mechanism of HA crystallites after burial proceeds homogeneously with time is not granted over very long periods when the earth crust has been subjected to important changes of the chemico-physical variables (temperature, pressure, acidity/alkalinity, etc.) which are not equally reproduced in the sites of specimens collection. Second, the determination of the average crystallite size may not always reflect properly the real effects of a distribution of the crystallite

sizes. In practice we assume that the average of a distribution is representative of the behaviour of various specimens that may have different size distributions.

Given the impossibility of receiving natural sample bones having certified only pure ageing effects without any contribution from mineralization processes, to further improve the reliability of the diffraction results in this specific subject the scientist has at least two ways available:

i) reduce the experimental uncertainty of intensity data points in the patterns with a more powerful X-ray source like at a synchrotron station;
ii) increase the number of specimens sampled across various ages.

Keeping the above limitations in mind and combining the knowledge of the fluoritisation process, it should be possible to arrive to estimate the age of bones from XRD only considering a very broad time scale such as that inspected here.

An alternative line of investigation should consider the study of fossil teeth, which are expected to be less biased by the contribution of authigenic minerals. Minimizing the mineralization effects should give emphasis to the ageing effect *per se*. Note that in our recent study about the microstructure of human teeth we have found crystallite size average values for HA systematically higher than in bones on account of different mechanical properties (Piga et al., in press).

Acknowledgements

The authors thank Angel Galobart, Jordi Galindo Torres, Laura Celià Gelabert (Institut Català de Paleontologia), Tim Thompson (University of Teesside), Piero Bartoloni and Michele Guirguis (University of Sassari) for supplying the osseous materials employed in this study.

G. Piga thanks Prof. Andrea Montella, Vittorio Mazzarello (University of Sassari) and the Sardinia Autonomous Region for financial support of "*Master and back*" project *TS160*.

References

Astibia, H., Payros, A., Suberbiola, X., Berreteaga, A., Elorza, J., Extebarria, N., Tosquella, J., 2005. Sedimentology and taphonomy of sirenian remains from the Middle Eocene of the Pamplona Basin (Navarre, western Pyrenees). Facies 50, 463–475.

Bartsiokas, A., Middleton, A.P., 1992. Characterization and dating of recent and fossil bone by X-ray diffraction. Journal of Archaeological Science 19, 63–72.

Chipera, J.S., Bish, D.L., 1991. Applications of X-ray diffraction crystallite/strain analysis to seismosaurus dinosaur bone. Advances in X-ray 34, 473–482.

Dollase, W.A., Reeder, R.J., 1986. Crystal structure refinement of huntite, $CaMg_3(CO_3)_4$, with X-ray powder data. American Mineralogist 71, 163–166.

Elliott, J.C., Mackie, P.E., Young, R.A., 1973. Monoclinic hydroxyapatite. Science 180, 1055–1057.

Elorza, J., Astibia, H., Murelaga, X., Pereda-Suberbiola, X., 1999. Francolite as a diagenetic mineral in dinosaur and other Upper Cretaceous reptiles fossil bones (Laño, Iberian Peninsula): microstructural, petrological and geochemical features. Cretaceous Research 20, 169–187.

Farlow, J.O., Argast, A., 2006. Preservation of fossil bone from the pipe creek sinkhole (late Miocene, Grant County, Indiana, U.S.A.). Journal of the Paleontological Society of Korea 22, 51–75.

Goodwin, M.B., Grant, P.G., Bench, G., Holroyd, P.A., 2007. Elemental composition and diagenetic alteration of dinosaur bone: distinguishing micron-scale spatial and compositional heterogeneity using PIXE. Palaeogeography, Palaeoclimatology, Palaeoecology 253, 458–476.

Handschin, R.G., Stern, W.B., 1992. Crystallographic lattice refinement of human bone. Calcified Tissue International 51, 111–120.

Hubert, J.F., Panish, P.T., Chure, D.J., Prostak, K.S., 1996. Chemistry, microstructure, petrology, and diagenetic model of Jurassic dinosaur bones, Dinosaur National Monument, Utah. Journal of Sedimentary Research 66, 531–547.

Hughes, J.M., Cameron, M., Crowley, K.D., 1989. Structural variations in natural F, OH, and Cl apatites. American Mineralogist 74, 870–876.

Lutterotti, L., Ceccato, R., Dal Maschio, R., Pagani, E., 1998. Quantitative analysis of silicate glass in ceramic materials by the Rietveld method. Materials Science Forum 278–281, 87–92.

McConnell, D., 1973. Apatite: Its Crystal Chemistry, Mineralogy, Utilization, and Geologic and Biologic Occurrences. Wien, Heidelberg, Springer, New York.

Michel, V., Ildefonse, Ph, Morin, G., 1996. Assessment of archaeological bone and dentine preservation from Lazaret Cave (Middle Pleistocene) in France. Palaeogeography, Palaeoclimatology, Palaeoecology 126, 109–119.

Perdikatsis, B., 1991. X-ray powder diffraction study of francolite by the Rietveld method. Materials Science Forum 79, 809–814.

Person, A., Bocherens, H., Saliège, J.F., Paris, F., Zeitoun, V., Gérard, M., 1995. Early diagenetic evolution of bone phosphate: an X-ray diffractometry analysis. Journal of Archaeological Science 22, 211–221.

Person, A., Bocherens, H., Mariotti, A., Renard, M., 1996. Diagenetic evolution and experimental heating of bone phosphate. Palaeogeography, Palaeoclimatology, Palaeoecology 126, 135–149.

Piga, G., Malgosa, A., Mazzarello, V., Bandiera, P., Melis, P., Enzo, S., 2008a. Anthropological and physico-chemical investigation on the burnt remains of Tomb IX in the "Sa Figu" hypogeal necropolis (Sassari, Italy) – early Bronze age. International Journal of Osteoarchaeology 18, 167–177.

Piga, G., Malgosa, A., Thompson, T.J.U., Enzo, S., 2008b. A new calibration of the XRD technique for the study of archaeological burnt remains. Journal of Archaeological Science 35, 2171–2178.

Piga, G., Thompson, T.J.U., Malgosa, A., Enzo, S. The potential of X-ray diffraction (XRD) in the analysis of burned remains from forensic contexts. Forensic Science International, in press, doi:10.1111/j.1556-4029.2009.01037.x. Available online at: www.blackwell-synergy.com.

Rietveld, H.M., 1967. Line profiles of neutron powder-diffraction peaks for structure refinement. Acta Crystallographica 22, 151–152.

Rushdi, A., McManus, J., Collier, R.W., 2000. Marine barite and celestite saturation in seawater. Marine Chemistry 69, 19–31.

Sillen, A., Parkington, J.E., 1996. Diagenesis of bones from Elands Bay Cave. Journal of Archaeological Science 23, 535–542.

Stathopoulou, E.T., Psycharis, V., Chryssikos, G.D., 2008. Bone diagenesis: new data from infrared spectroscopy and X-ray diffraction. Palaeogeography, Palaeoclimatology, Palaeoecology 266, 168–174.

Sudarsanan, K., Mackie, P.E., Young, R.A., 1972. Comparison of synthetic and mineral fluorapatite, $Ca_5(PO_4)_3F$, in crystallographic detail. Materials Research Bulletin 7, 1331–1338.

Sudarsanan, K., Young, R.A., 1978. Structural interactions of F, Cl and OH in apatites. Acta Crystallographica 34, 1401–1407.

Trueman, C.N.G., Behrensmeyer, A.K., Tuross, N., Weiner, S., 2004. Mineralogical and compositional changes in bones exposed on soil surfaces in Amboseli National Park, Kenya: diagenetic mechanisms and the role of sediment pore fluids. Journal of Archaeological Science 31, 721–739.

Weiner, S., Bar-Yosef, O., 1990. States of preservation of bones from prehistoric sites in the Near East: a survey. Journal of Archaeological Science 17, 187–196.

Wings, O., 2004. Authigenic minerals in fossil bones from the Mesozoic of England: poor correlation with depositional environments. Palaeogeography, Palaeoclimatology, Palaeoecology 204, 15–32.

Wopenka, B., Pasteris, J.D., 2005. A mineralogical perspective on the apatite in bone. Materials Science and Engineering C 25, 131–143.